Diagnostics of a nanosecond atmospheric plasma jet. I. Electron and ro-vibrational excitation dynamics

Nikolay Britun[1], Peterraj Dennis Christy[1], Vladislav Gamaleev[1,2], Masaru Hori[1]
[1] *Center for Low-temperature Plasma Sciences, Nagoya University, Chikusa-ku, 464-8603 Nagoya, Japan and*
[2] *The present address: Air Liquide Laboratories, 2-2 Hikarinooka, 239-0847 Yokosuka, Japan*

Atmospheric repetitive He discharge with 10 ns current peak width and $3{\cdot}10^{11}$ V/s voltage front rise working in jet geometry is studied. The *first* part is devoted to electrical and optical discharge characterization including voltage-current behavior, emission dynamics, as well as ro-vibrational dynamics of N_2, N_2^+ and OH molecules. It is found that He atoms get excited at the very early stage, as a result of ionization wave formation. This process follows by the excitation of O, N_2 and N_2^+. It is also shown that a rather small (0.1-1 %) air admixtures facilitate gas breakdown, as revealed by shortening of the discharge current risetime. The rotational excitation of N_2^+ always overtakes He excitation by about 5 ns, with rotational temperature peaking at about 650 K and decaying afterwards, whereas rotational temperature of N_2 always remains constant equal to about 300 K. This value is associated with gas kinetic temperature since the electron-rotational (e-R) excitation process is too slow, so it cannot be activated during the plasma phase additionally altering rotational excitation of N_2. Nitrogen molecules remain vibrationally excited in the discharge, post-discharge and jet areas after the plasma pulse which is likely a result of ionization wave propagation. Upon water vapor injection the apparent OH rotational distributions reveal double Boltzmann slope representing thermalized and non-thermalized OH groups. Rotational temperature of the thermalized group correlates with the one of N_2^+ showing, however, much longer relaxation time, whereas for the non-thermalized group it remains above 1 eV at all conditions.

The obtained results confirm that the studied ns- discharge is a good candidate for temperature-sensitive applications, such as the bio-sample treatment. Further analysis related to the ionization waves, electron density and electric field behavior is undertaken in the Part II.

Keywords: nanosecond discharge, jet, ionization waves, low-temperature plasma, optical emission spectroscopy, rotational temperature, vibrational temperature.
PACS numbers: 52.20.-j, 34.80.Gs, 52.70.-m, 33.20.Sn, 33.20.Tp, 78.47.D-.

I. INTRODUCTION

Selective delivery of chemically active species on a surface at low temperature and at atmospheric pressure represents a challenge, both fundamentally and technically. Based on the previous studies the solution looks evident: discharge non-equilibrium is a key point for remote plasma chemistry when the efficient ionization and molecular dissociation (radicals production) are favored, as a result of high energy separation between plasma electrons and heavy particles. In practice, however, in the non-equilibrium discharges the fast quenching of active species in the ambient air, non-negligible gas heating and remoteness of plasma core from a target represent certain obstacles.

In order to maintain plasma non-equilibrium the electron energy transfer to the kinetic motion of atoms and molecules should be avoided. Such transfer happens via the electron-translational (e-T), electron-vibrational (e-V) and vibrational-translational (V-T) energy exchange channels which are responsible for electron energy dissipation and gas heating [1, 2]. The vibrational-vibrational (V-V) exchange is also important, representing redistribution of vibrational excitation within the same or between different molecular species. These channels are particularly efficient in spark and arc plasma where the losses for gas heating are essential [2–4]. The formation of sparks/arcs in the discharge can be avoided if plasma duration is shorter than the process characteristic time. This time is lying in the ns range, as the so-called glow-to-spark transition is a matter of hundreds ns typically [5]. If this condition is fulfilled, the electron energy should not be dissipated to translational gas motion, preserving non-equilibrium.

In the discharges with ns- pulse duration (term ns- discharges is used below), where fast voltage rise between electrodes (during several ns) and high voltage peaks (tens or even hundreds kV) take place, two fundamental physical phenomena may happen: the runaway electron beam propagation [18, 19] and, as a result of electron deceleration in the gas [20], the generation of X-ray radiation [21]. The former effect had been suggested in thunderclouds by Wilson [22, 23] nearly a century ago, provoking the further studies on this topic. Now it is known [19] that the runaway electron generation depends on electron multiplication conditions in the gas, in particular the mean free path, requiring very high voltage between electrodes (roughly 200 kV for He) [24].

At relatively low applied voltage peaks runaway electrons are not generated, however, the propagation of the so-called fast ionization waves (FIWs) may still takes place. The FIW propagation velocity may range from about 10^3 to 10^5 m/s (when homogeneous electric field dominates) or be much higher (up to $\sim 10^8$ m/s), at the

TABLE I. Selected applications of the repetitive ns- discharges in various geometries.

Application	Pressure used	discharge geometry	Diagnostics [a]	Reference
Ignition	3 atm.	planar	various	[6]
Ignition, combustion	1 atm.	coaxial, etc.	various	[7]
Engines (ignition)	1 atm.	capacitive	electrical only	[8]
Flow control	1 atm.	dielectric barrier	simulation	[9]
Water purification	1 atm.	dielectric barrier	OES, gas analyzer	[10]
NO_x reduction	1 atm.	coaxial	gas analyzer	[11]
Nitrogen fixation	1 atm.	water-contacting	OES, LIF, TALIF	[12]
CO_2 reduction	1 atm.	pin-to-pin (cavity)	GC	[13, 14]
Surface treatment	1 atm.	jet	OES	[15]
Biomedical	1 atm.	jet	OES	[16]
Biomedical	1 atm.	jet	LIF, OES	[17]

[a] The abbreviations used: OES - optical emission spectroscopy; LIF - laser-induced fluorescence; TALIF - two photon absorption LIF; GC - gas chromatography.

final stages of breakdown [25]. In general, the propagation velocity is higher when gas is preionized to a higher extent or if the voltage rises more rapidly. At lower applied voltages front velocity decreases, roughly scaling with the voltage peak value [25]. Experimentally FIW propagation in the ns- discharges has been studied in the numerous works [15, 26–31].

The repetitively pulsed ns- discharges have high application potential in several important domains, such as combustion ignition [6, 7, 32], surface treatment [15], flow control [9], molecular pollutant degradation [10] as well as in gas reforming, including CO_2 conversion [13, 14], nitrogen fixation [12] and NO_x compounds reduction [11], as briefly summarized in Table I. Mainly CO, NO_x and O radicals were in focus so far [12–14, 33], including a comparative study of O and NO density by laser-based methods [12] and CO quantification by gas chromatography [13, 14]. The advantages of burst pulse regime leading to higher selectivity in gas conversion [14] and higher radical density [12] have also been demonstrated.

Depending on the application ns- discharges can operate in various geometries, starting from low-pressure gaseous diodes [26, 27, 34], and ending up by the dielectric barrier discharge (DBD) [10], capacitive [33], pin-to-pin [13, 14, 35], coaxial [11, 36], water-contacting [12] and finally jet geometry with both internal [37–39] and surrounding the tube [15, 40–43] electrode configurations. The variety of jet geometries are discussed by Lu et al. [44] and by Morabit et al. [45].

In the case when the ionization waves are channelized into the open air, as suggested in early works [18], the discharge resembles a plasma jet when ionization wavefronts protruding into the open air and possessing high-energy electrons, high electric field and revealing non-equilibrium [25]. Mainly for this reason, as well as due to the low gas temperature [46], the ns- jet discharges are attractive for (distant) treatment of the temperature-sensitive samples, such as tissues, plants, etc. In particular, the biomedical ns- jet applications were in focus of researches during last decades [16, 45, 47], including commercial devices for medical treatment [47].

During two recent decades numerous studies devoted to the short (sub-μs) pulsed He-based plasma jets and their physical properties were published, dealing with several effects such as gas heating [46, 48], electron temperature and density [37, 49–51], the role of gas admixtures [43, 52], as well as the ionization waves, in particular their structure [29, 53] and propagation dynamics [30, 31]. Some works are focused on the applied (high-) voltage and electric field dynamics in the discharge [54, 55], as these parameters are critical for understanding of the ns- discharge physics, such as gas breakdown, ionization wave propagation and related phenomena. A significant part of this understanding is also coming from the AC- (alternative current) [40, 56, 57] and RF- (radiofrequency) [42, 58] driven plasma jets.

In spite of large number of studies related to He-based ns- jet geometry, they are often focused on only few plasma parameters for a given geometry, and those dealing with multiple diagnostics are rather limited. The number of works focused on the short (< 10 ns) pulsed discharges and combining multiple discharge parameters in one study is further limited. There are also inevitable spatial limitations for the applied diagnostics: e.g. some excellent diagnostic works related to laser-based techniques deal only with the jet (i.e. gas effluent) area, as it is not covered by any electrodes or dielectric tubes and laser-based methods can be implemented easily [49–51, 59, 60], whereas the inter-electrode space and tube areas remains in shadow.

Regarding the above-mentioned, the goal of this work was to characterize a short-pulsed (10 ns) jet discharge in several zones (such as inter-electrode space, dielectric tube and effluent) using the same discharge geometry and close operation conditions. Our work is targeted to the multiple plasma parameters measured, whenever possible, in both the time- and space- domains. The first part of this study is focused on the dynamics of elec-

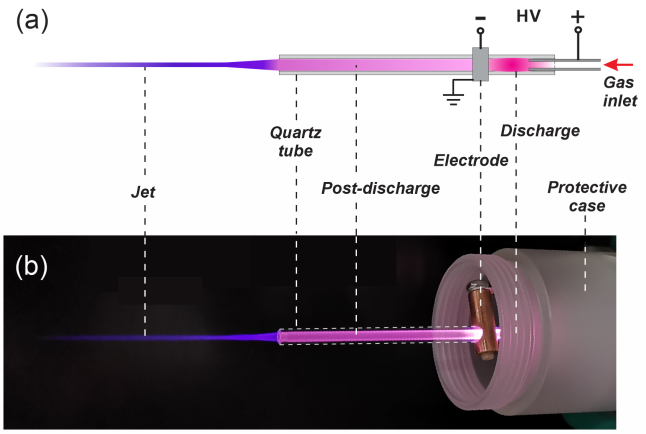

FIG. 1. The scheme (a) and the photograph (b) of the ns- jet discharge used in this work (appearance in pure He is shown). HV denotes high voltage.

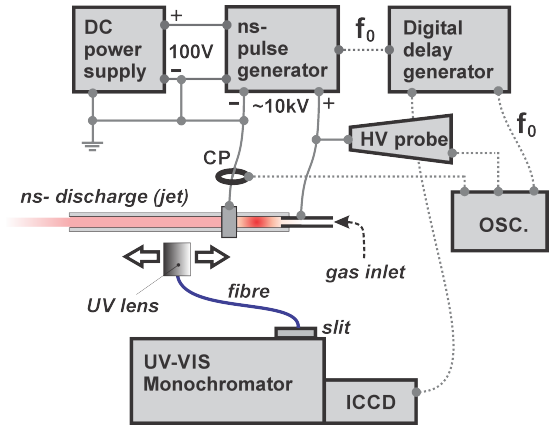

FIG. 2. Electrical schematics of the ns- discharge, including a direct current power supply, ns- pulse generator, digital delay generator, the jet assembly itself, and the monochromator with ICCD. f_0 denotes discharge pulse repetition rate (600 Hz typically). The abbreviations used: DC - direct current, CP - current probe, HV - high voltage, OCS. - oscilloscope, ICCD - intensified charge coupled device.

trical discharge parameters (current, voltage), emission line intensity, and ro-vibrational excitation of the relevant molecules (N_2, N_2^+ and OH), whereas the second part is dealing with ionization wave propagation dynamics, electron density and electric field measurements in the same discharge geometry at similar discharge conditions. The work also discusses the effects induced by the small air and water vapor admixtures to He gas flow. Another distinctive feature of this study is the implementation of a custom ns power supply, which is designed based on a single thyristor circuitry, thus representing an inexpensive solution for ns pulse generation [61]. The proposed scheme assures high plasma pulse repeatability essential for long time operation and stable time-resolved diagnostics.

The Part-I is organized as follow: after the experimental details the current/voltage waveform behavior is discussed, which is followed by the discussion on the emission lines behavior, rotational and vibrational excitation dynamics of the selected molecules, and conclusions.

II. EXPERIMENTAL

A. The ns- discharge

1. *Discharge setup*

The studied ns- discharge has been developed in our Lab. and composed of a custom-design ns pulse generator based on an inductive energy storage circuit with a single 4 kV static induction thyristor [62]. A single thyristor approach provides numerous benefits including high discharge repeatability and high overall robustness. Also, the ability of plasma ignition by an external trigger in implemented, when the pulse repetition rate (PRR) in a wide range can be used. For this work the discharge scheme has been adapted to jet geometry, as shown in Fig. 1, in which the repetitive 10 kV voltage pulses with the voltage growth rate of about $3{\cdot}10^{11}$ V/s were produced by the ns pulse generator. The further details can be found elsewhere [61].

The circuitry of the ns jet discharge was powered by a commercial direct current (DC) power supply and a lab-made ns pulse generator, as shown in Fig. 2. The plasma pulse has been triggered using external TTL (transistor-transistor logic) signal passing via Toshiba TLP2955 optocoupler, used for the sake of trigger unit protection. A Princeton Instrument DG645 delay generator has been used for the PRR control and synchronization with the detection system. A closed-loop water cooling system rated for up to 360 W of power dissipation has been used for cooling of the active components. 100 V of DC voltage and 0.2 A of DC current were typically consumed making the total DC consumed power of about 20 W, when PRR is 600 Hz.

The jitter at the output of the ns pulse generator relatively to the external TTL clock was about 3 ns. This value is likely related to poor gas breakdown repeatability, both in time and space [63]. The wide PRR range, from about 50 Hz to 2.5 kHz has been explored showing no long-term current/voltage drift and stable discharge performance. At lower repetition rate the system experienced further jitter increase, as a result of longer off-time and poorly repetitive breakdown, whereas the values of PRRs > 2.5 kHz were avoided to prevent overheating. In the most cases, unless stated otherwise, the PRR was limited to 600 Hz.

In our geometry a high voltage (positive) electrode in the form of metal tube is placed into the quartz tube, whereas a hollow (grounded) electrode is surrounding the quartz tube (see Figs. 1 and 2). The alternative electrode

TABLE II. Main operation parameters of the ns- discharge.

Parameter	Value/range
Voltage peak [a]	10 kV [b]
Voltage growth rate	$\sim 3{\cdot}10^{11}$ V/s
Current peak range	2.5 - 6 A
Voltage FWHM [a]	$\sim$150 ns [b]
Current FWHM [a]	$\sim$10 ns
Current pulse jitter	3 ns
Pulse repetition rate	0.05 - 2.5 kHz
DC consumed power [c]	20 W
Distance between electrodes	$\sim$10 mm
Quartz tube length	35 mm
Quartz inner diameter	2 mm
Gas used	99.999 % He
Admixtures used	dry air, water vapor
He gas flow	2 slm
Gas velocity in the tube [d]	$\sim$10 m/s

[a] - a typical value.
[b] - voltage peak is higher and narrower without load.
[c] - estimated at PRR = 600 Hz.
[d] - at 2 slm of the gas flow and T = 300 K.

TABLE III. Spectroscopic and electric tools used in this study.

Tool/characteristics	Name/parameters
Monochromator 1	SOL Instruments MSDD1000
Effective focal length	1 m
Gratings used	1800, 2400 groove/mm
Min. slit width	40 μm
Spectral resolution	about 18 pm
ICCD detector	Andor DH340-18U
Gate width used	3-200 ns
Monochromator 2	Acton 750
Focal length	0.75 m
Gratings used	2400 groove/mm
Min. slit width	20 μm
Spectral resolution	about 21 pm
ICCD detector	Andor DH734-18U
Gate width used	3-50 ns
Collecting optics	Nikon 105 mm f/4.5 UV + fibre
Clock generator	Stanford Instruments DG645
Current probe	Pearson (Model 2877)
Voltage probe	Tektronix P6015A
Oscilloscope	Tektronix DPO4054

polarity was not tested. The grounded electrode, the negative output of DC generator and the high voltage probe were grounded to the same point, see Fig. 2. A constant He gas flow of 2 slm (standard liter per minute) mixed with air or/and water vapor has been supplied to the gas inlet of the discharge tube. The dry air flow has been changed in the range from 2 sccm (standard cubic centimeter per minute) to 200 sccm. The digital mass flow controllers were implemented in each channel. The main working parameters are summarized in Table II.

2. *Water vapor injection*

For water vapor injection into the discharge area a dedicated vaporizer has been implemented. The water temperature in the vaporizer volume has been kept equal to 45 °C. The vapor produced in this way has been mixed with a separate He flow (controlled by a digital mass flow controller) and delivered to the discharge volume along with the other gases. He flow was introduced above the water level, so no bubbling effect has been used. Since the amount of water vapor delivered to the discharge area was not calibrated in this work, the relative units called 'vapor units' (v.u.) are introduced. By definition, 1 v.u. = 1 sccm of He mixed with water vapor produced in the evaporator volume at 45 °C. As a result of water vapor addition a steep increase of the OH (A-X, 0-0) band emission intensity has been clearly registered indicating OH radicals formation. The emission intensity increases nearly linearly at small vapor additions and peaks at about 50 v.u. Afterwards it decays gradually, likely as a result of the elevated quenching of the OH(A) excited state by H_2O, OH and O_2 molecules (see the supplementary data, Fig. S1).

B. The diagnostic tools and methods

1. *Electrical measurements*

A Tektronix P6015A high voltage probe has been used for voltage monitoring, whereas the discharge current was measured by a Pearson Model 2877 current monitor with 2 ns of risetime, 200 MHz of the bandwidth and 100 A of the current limit. A Tektronix DPO4054 digital oscilloscope has been used for the waveform visualization and data storage. Due to the unknown signal delay in the current probe and in the optical detectors used, the moment of the current peak appearance was not correlated exactly to the optical emission signal. The related questions are discussed in the Part II.

2. *Spectroscopic tools*

Either an Acton-750 monochromator equipped with an Andor DH734-18U intensified charge coupled device (ICCD) camera (sensitive in the ultraviolet (UV) range) or a SOL Instruments MSDD1000 double dispersion monochromator with an Andor DH340-18U ICCD (sensitive in the visible (VIS) range) were used in this work for spectral measurements. Both ICCDs were controlled by the Andor Solis software (v. 4.32). Depending on required resolution, the diffraction gratings with either 1200, 1800 or 2400 groove/mm were implemented;

while the monochromator entrance slit width was ranging from 10 μm to 100 μm. The final spectral resolution from about 0.02 nm to 0.1 nm was obtained. A schematic arrangement of the monochromator with a fiber, UV lens and ICCD detector is shown in Fig. 2.

Both ICCD detectors were operating in the accumulative mode where the optical gate starting from 3 ns wide has been used. The number of accumulations has been typically varying from 10 to 100, depending on the measurement type. For instance, up to 100 accumulations were typically required for rotational bands measurements. The light has been collected via a Nikon 105 mm f/4.5 UV imaging lens directly connected to the optical fibre and then to the monochromator. The UV-VIS optical fibre with a rectangular aperture at the both edges has been used. Such fibre configuration allowed collecting light from an elongated volume matching the entrance slit of monochromator at the same time. The detailed list of the spectroscopic and electrical tools are given in Table III.

For all the time-resolved measurements the time scale has been fixed in the same way, making the He emission peaks (which all behave similarly) appearing at 20 $\pm$2 ns of the delay time. Its consistency has been verified before each time-resolved measurement.

3. *Ro-vibrational spectroscopy*

Three optical transitions were used for rotational excitation analysis, namely: N_2 ($C^3\Pi_u^+ \rightarrow B^3\Pi_g^+$) , N_2^+ ($B^2\Sigma_u^+ \rightarrow X^2\Sigma_g^+$) and OH ($A^2\Sigma^+ \rightarrow X^2\Pi^+$) with the v'=0 $\rightarrow$ v"=0 vibrational transitions in each case [64]. Rotational spectra were acquired using either the SOL or the Acton monochromators (see Table III) with a 2400 groove/mm diffraction grating providing spectral resolution of about 25 pm.

For determination of rotational temperature (T_{rot}) the experimental rotational spectra were compared to the ones synthesized at different T_{rot} values using freely available codes (Massive OES [65–67] in the case of N_2 and LIFBASE [68] in the case of N_2^+). In the N_2 and N_2^+ cases this process includes minimization of fitting residue between the synthesized and the experimental spectra using a custom made code (in the Mathematica 12.0 package). The error of this method depends on the signal-to-noise ratio (SNR) of the experimental data as well as on the temperature step used for spectra calculation. Since the last factor is decisive, the error of T_{rot} determination in our case is about 25 K at low temperatures and about 50 K when T_{rot} exceeds 600 K.

Since rotational distributions in the OH case reveal double Boltzmann slope, a two-temperature fit has been used. For this purpose spectra fitting has been performed using Boltzmann Plot option in the Massive OES package, capable of restoring rotational distribution from a rotational spectrum [67]. The T_{rot} error in this case is equal to the Boltzmann plot fitting error. A fitting example for the N_2^+ rotational band is given in Fig. 3, from where the difference in the rotational bands appearance is evident at two shown time delays (fitting examples for the N_2 and OH bands are given in the supplementary data, Fig. S2 and S3).

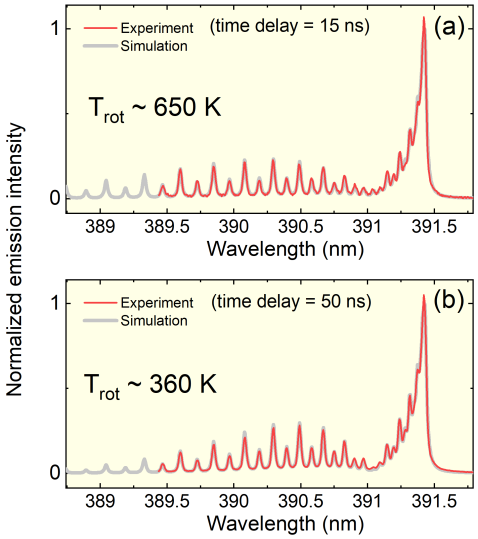

FIG. 3. Rotational spectra corresponding to the N_2^+ (B-X, 0-0) transition acquired during (a) and after (b) the plasma current peak. The rotational temperatures obtained as a result of comparison with synthesized spectra indicate higher rotational excitation of N_2^+ during plasma pulse.

Additionally, the vibrational temperature (T_{vibr}) of the N_2 ($C^3\Pi_u^+$) state has been examined for several discharge conditions (using 1800 groove/mm grating and 100 μm of the slit width). Two vibrational bandhead sequences with v'-v" = -2 and -3 were involved and an average between them has been taken as a final T_{vibr} value. During this procedure three to four vibrational bandheads were used to deduce T_{vibr} value. A Boltzmann distribution for the N_2(C) vibrational states has been assumed, as in the previous works [69]; the corresponding spectral constants for N_2 were taken from Lofthus and Krupenie [70]. The vibrational bandhead intensities were additionally corrected to the spectral response of the system.

III. PLASMA CORE ANALYSIS

A. Electrical characteristics

Based on electrical measurements, each plasma pulse of the ns- discharge represents a sharply changing current appearing at the moment of breakdown, after the applied voltage exceeds threshold value (of about 10 kV). In general, the moment of gas breakdown is not a repeatable process as streamer propagation path and voltage growth are not repeatable. In our case the use of induction energy storage circuit allowed to supply large current value

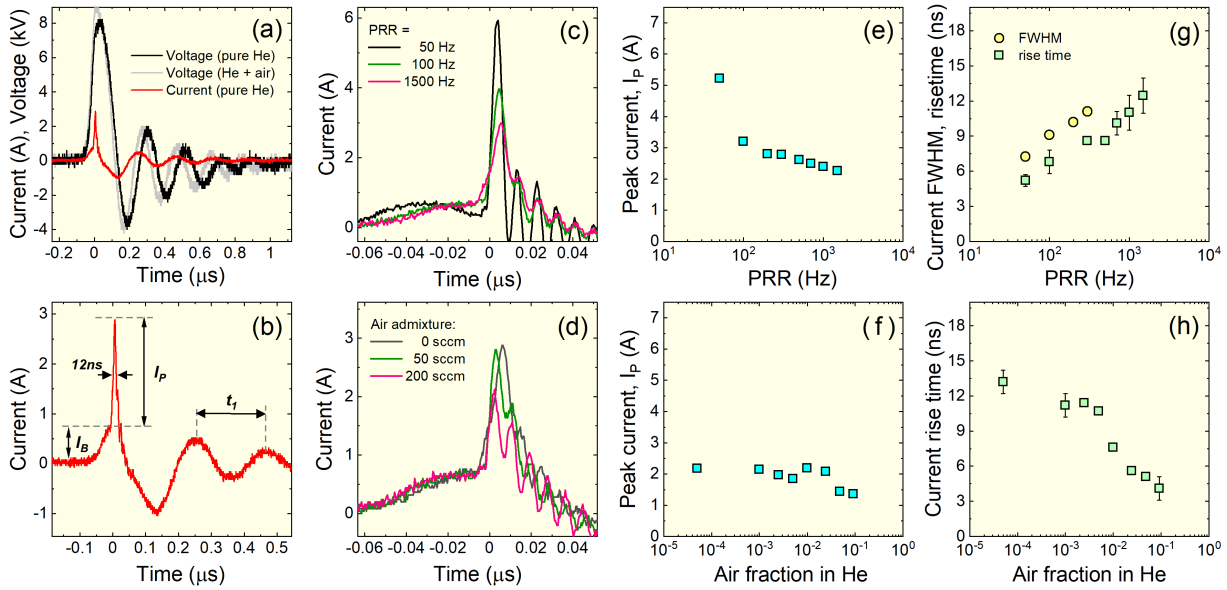

FIG. 4. Summary of the current and voltage waveform behavior illustrating: (a) general voltage and current evolution; (b) magnified current evolution; the effects of PRR (c) and air admixture (d) on the current profile; the peak current as a function of PRR (e) and air admixture (f); the current peak width and risetime as a function of PRR (g) and air admixture (h).

during a short time so the discharge current developed in a form of an avalanche-like sharp peak with the FWHM (full width at half maximum) of about 10 ns, whereas the voltage peak is much wider (about 150 ns), as shown in Fig. 4(a,b).

The voltage applied to the load is mainly dictated by the internal circuit current pulse supplied by the thyristor and the load capacitance leading to the voltage increase on the electrodes and the breakdown itself (at the threshold voltage). After the breakdown and a sharp current peak appearance a capacitively-coupled plasma (CCP) is formed owing to the damping oscillations generated by the LCR (inductance-capacitance-resistance) resonance between the internal components of the ns generator, accompanied by a displacement current between the electrodes. Several oscillations of the CCP discharge are visible in Fig. 4(a-d) with the displacement current appearing $\pi/2$-shifted with respect to the voltage, see Fig. 4(a). The characteristic time t_1 of the voltage and current oscillations corresponds to about 5 MHz (Fig. 4(b)). This frequency is likely defined by the internal components of the ns pulse generator, however, plasma impedance may be important as well, which is confirmed by a small frequency increase when air is added to the gas mixture (gray curve in Fig. 4(a)).

The observed dumping oscillations, in turn, are caused by a fast circuit switch during the nanosecond pulse formation. The internal circuit in ns generator operates close to LCR resonance, in order to maximize the output voltage, at the same time resulting in amplification of the observed dumping oscillations [61]. We can also see that a certain current growth precedes the current peak. This small current, denoted as basement current (I_B) in Fig. 4(b), is likely a result of preliminary discharge formation before the breakdown (i.e. corona or Townsend discharge) [71, 72].

At low PRR the current peak (I_P) increases significantly, as shown in Fig. 4(c, e), which is accompanied by a decrease in the peak FWHM and shortening its risetime, see Fig. 4(g). These effects point out on a harder breakdown conditions at low PRRs when the number of the charge carriers at the moment of breakdown is significantly smaller as compared to the high repetition rates. Note, that the current pulse width of about 7 ns is achievable at low PRR corresponding to current risetime of only 5 ns, as shown in Fig. 4(g). A nearly threefold increase in the current risetime is observed at 2 kHz. The preionization in the discharge volume might be a key factor for the observed effects, since at low PRR the breakdown happens at higher voltages, due likely to the presence of fewer charge carriers in the afterglow. Higher voltage corresponds to a larger charge stored in the load capacitance which may contribute to the initial current surge during the discharge stage, resulting in the elevated current values and shorter risetime at low PRR.

The influence of air and water vapor admixtures on the current evolution are different: the current peak somewhat decreases at higher air admixtures, as shown in Fig. 4(d,f), remaining almost insensitive to the water admixture (not shown). At the same time, the more air is admixed the faster current rise is detected, as shown in Fig. 4(d, h). Thus, gas breakdown in the presence of air is faster, which is likely a result of vibrational excitation of N_2 and O_2 at the beginning of the breakdown, which also facilitates ionization (e.g. via $N_2(v) + e \rightarrow N_2(v+1) + e$; $N_2(v) + N_2(v) \rightarrow N_2^+ + N_2$, with (v)

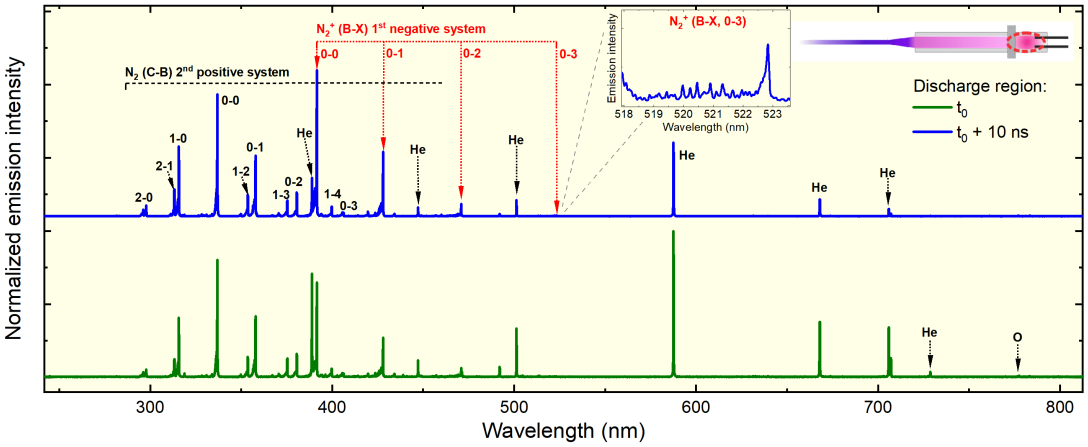

FIG. 5. Emission spectra taken in the discharge area at the moment corresponding to the He emission peak, t_0 (green line), and 10 ns after the peak (blue line). He with 0.1% of air admixture is used. Intensity is normalized to 1.

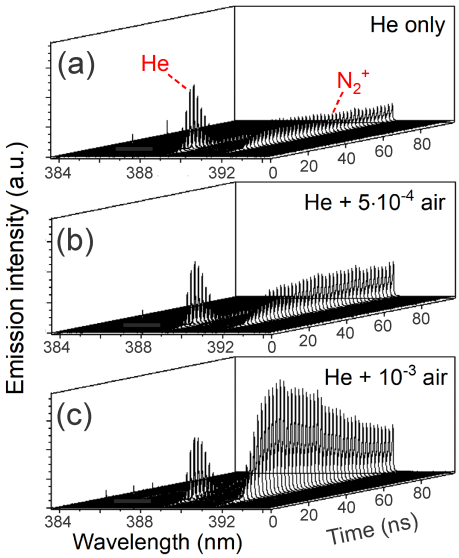

FIG. 6. Time evolution of the He (388.86 nm) emission line and N_2^+ (B-X, 0-0) emission bandhead (391.4 nm) in pure He (a) as well as with 0.05% (b) and 0.1% (c) of dry air admixtures. Same scale is used for intensity axis in each case.

denoting vibrationally excited states; mind also similar reactions with $O_2(v)$). These observations emphasize the role of N_2, and other N-containing (vibrationally excited) molecules in the breakdown evolution. Vibrationally excited species most probably originate from the previous plasma pulse, as the plasma duration is too short for efficient e-V energy transfer within the same pulse, as shown below.

B. Emission dynamics

The voltage growth rate realized in our system (about 0.3 kV/ns) leads to ionization wave propagation in the discharge tube, corroborating with the previous works [25, 30, 53, 73]. In this paper FIW propagation is confirmed by He and N_2 emission dynamics in the post-discharge. A detailed analysis is undertaken in the Part II [74].

The He emission lines along with the ones of N_2 (from Second Positive System) and N_2^+ (from First Negative System) dominate the discharge spectra, as shown in Fig. 5, where two spectra acquired with 10 ns time interval are shown. We can also observe a significant increase in N_2^+ emission at longer time delay. This effect is further clarified in Fig. 6, where He emission dominates only during a short interval at the beginning, being overtaken gradually by the N_2^+ band. The N_2^+ emission evolves much slower than the one of He, also showing much longer decay time. Slow evolution may be related to the fact that e-V excitation channel is not activated during the plasma pulse [75].

The sharp He emission peak is likely a result of ionization front formation and (soon after) the electron avalanche. Even though the wavefront should precede the avalanche [27], these two events are divided by only bout 5-10 ns in our case [74]. The corresponding excited state of He ($3p\,^3P_J^o$), corresponding to 22.8 eV, requires high energy electrons for excitation. The strong collisional quenching at atmospheric pressure results in fast He emission decay afterwards. While hot electrons from the FIW wavefront can easily excite He, their energy and density might not be sufficient during the CCP time, resulting in a negligible He emission. At the same time, the emission of N_2^+ grows slowly and remains strong during much longer time, see Fig. 6, as the (low) electron energy may be channelized to N_2^+(B) excitation in this case. The metastable He atoms may also contribute to ionization of N_2, as suggested by Li et al. [76].

The He, N_2 and N_2^+ emission lines reveal a sharp first emission peak, shown in Fig. 7(a-c), as compared to the products of dissociation in plasma, such as OH, O and H, for which this peak is absent, see Fig. 7(d-f). In the

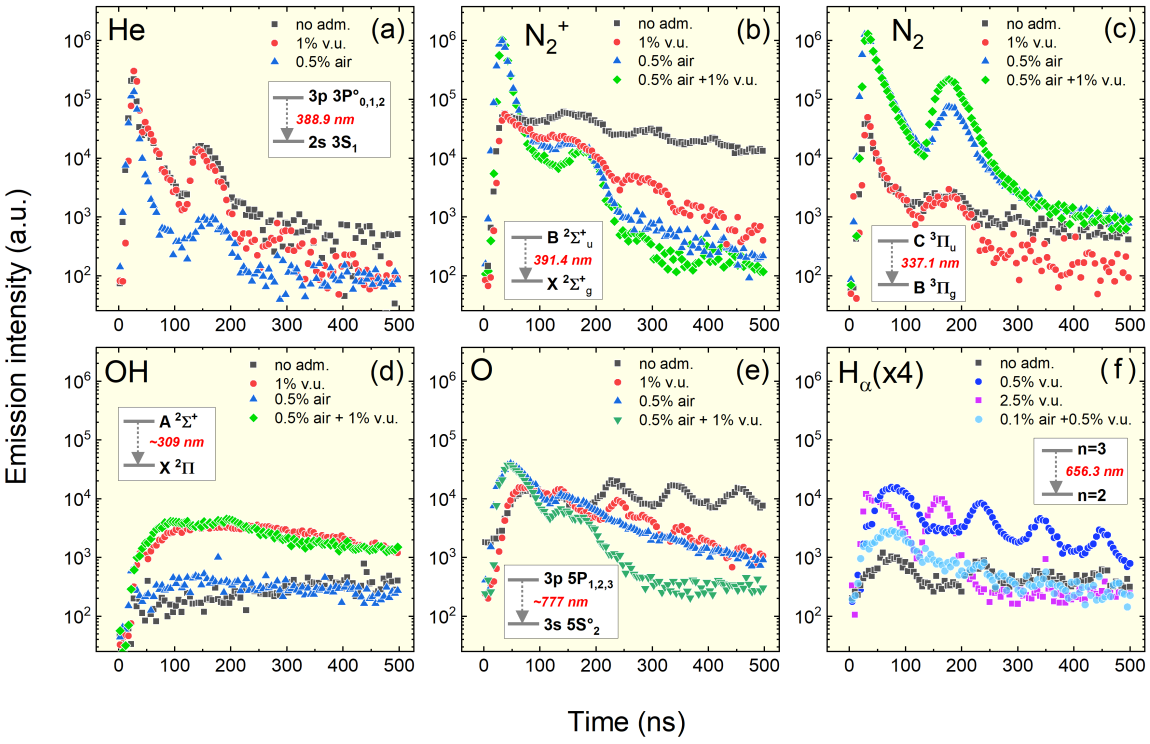

FIG. 7. Time evolution of the relevant emission peaks in the plasma region including He (a), N_2^+ (b), N_2 (c), OH (d), O (e) and H_α (f). Pure He as well as air and water vapor admixtures used are given in the legends. Data are corrected to the spectral response of optical system.

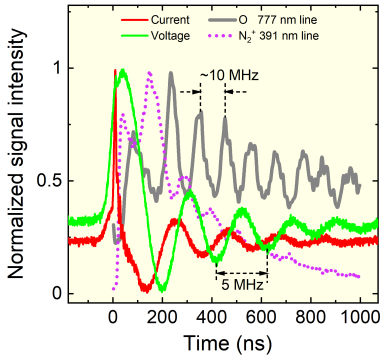

FIG. 8. Oscillations of the discharge current and voltage superimposed onto the time-resolved behavior of O and N_2^+ emission peaks demonstrating the emission oscillation at double frequency.

case of He a faster emission decay with air addition is evident, due to the stronger quenching, see Fig. 7(a). Note, that the emission decay with a small water vapor addition is similar to that obtained with pure He, signifying the presence of naturally admixed air in the last case. Both He and N_2 also reveal a weak and broad peak at about 150 ns (see Fig. 7(a,c)) likely related to the second (negative) current oscillation visible in Fig. 4(a,b). The intensity of He (N_2) secondary peak decreases (increases) upon the air addition (see supplementary data, Fig. S4). This process is also accompanied by a weak electron density peak in the discharge gap [74].

The decay of He emission line with and without air admixture enable determination of quenching rates of the He $(3p\,^3P_J^o)$ excited state. Neglecting the finite width of the current peak, rough estimation for the quenching rate coefficients yields: $k_q^{He}(\text{in He}) \approx 2{\cdot}10^{-12}$ cm^3/s and $k_q^{He}(\text{in air}) \approx 10^{-9}$ cm^3/s. Since the data related to quenching of He excited states is sparse, only few works were found reporting values for He ^{1}P state quenching by N_2 (about $4{\cdot}10^{-9}$ cm^{-3} [77]), as well as for He ^{3}P state quenching by He (about $7{\cdot}10^{-11}$ cm^{-3} [78]). The discrepancies with our result may be related to the presence of CCP discharge distorting pure exponential emission decay in our case. Based on Fig. 7(b,c), the quenching rate coefficients for N_2(C) and N_2^+(B) excited states in He can be estimated similarly. Taking the quenching rate coefficients of these states in N_2 and O_2 from [79] close values were found in both cases (about $2 \cdot 10^{-12}$ cm^3/s). No higher than a twofold discrepancy with the literature data is found in the case of N_2(C) state [80, 81], which is a reasonably good agreement. For comparison, the quenching rate coefficient of this state by O_2 is roughly two orders of magnitude higher [82], mainly defining quenching in dry air.

All the emission lines show much slower decay after 100 ns in Fig. 7, following the CCP plasma decay. The data in Fig. 8 clearly demonstrate that both the N_2 and

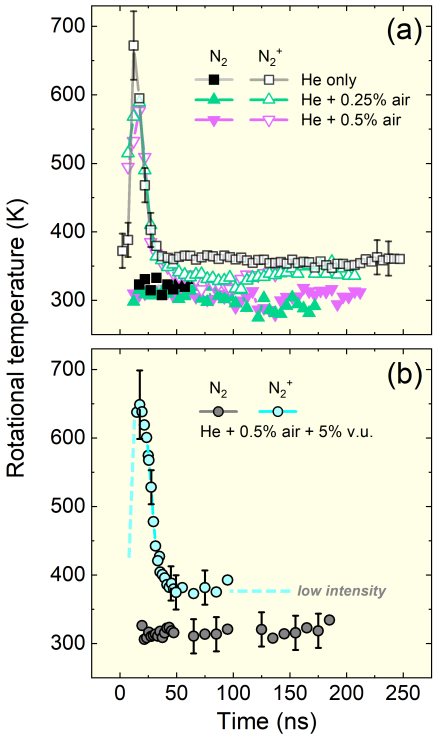

FIG. 9. Time-resolved behavior of rotational temperature in the plasma region withdrawn from the N_2(C-B, 0-0) and N_2^+(B-X, 0-0) rotational emission bands for air (a) and water vapor + air (b) admixtures. The gaps in the datapoints are the result of weak emission intensity.

TABLE IV. The rate coefficients (k) and characteristic time (τ) for the main energy exchange channels, estimated at T = 300 K.

Process	k (cm^3/s)	τ (ns)	Reference
T-T (He-He)	-	0.14	[82]
T-T (N_2-N_2)	-	0.13	[82]
R-T (N_2 - He)	$1.4{\cdot}10^{-10}$	0.3	[83]
R-T (OH - He)	$\sim 10^{-11}$	4-5	[84, 85]
e-R (N_2)	$2.3{\cdot}10^{-9}$	90 [a]	[75]
e-V (N_2)	$4.4{\cdot}10^{-9}$	45 [a]	[75]
V-T (N_2 - He)	$\sim 5{\cdot}10^{-18}$	$6{\cdot}10^6$	[82, 86]
V-T (N_2 - N_2)	$\sim 10^{-22}$	$>10^{10}$ [b]	[82, 87]
V-T (N_2 - O_2)	close to N_2-N_2	$>10^{10}$ [b]	[82]

[a] - electron density of $5{\cdot}10^{15}$ cm^{-3} is assumed [74].
[b] - estimated at 0.5 % of air admixture.

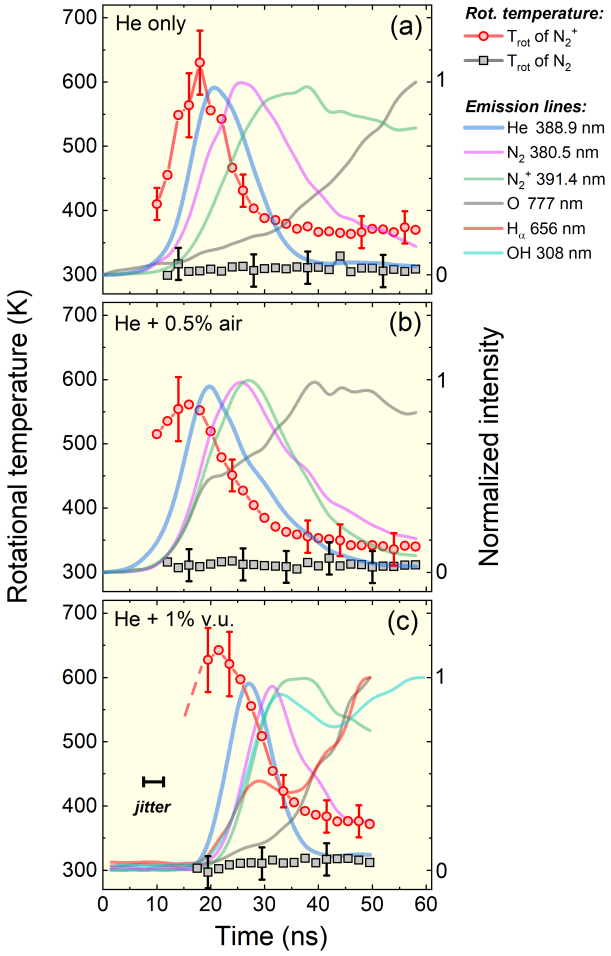

FIG. 10. Time-resolved evolution of T_{rot} of N_2 and N_2^+ along with the relevant emission peaks taken with 2 ns time step at the very beginning of the plasma cycle measured in pure He (a), He with 0.5% air (b), and He with 1% of water vapor units (c) admixtures. Time jitter shown is relevant for all sub-figures.

O emission peaks oscillate at a double frequency, as compared to that of the voltage/current oscillations, thus confirming the plasma excitation during each half-period in CCP discharge.

The emission dynamics is further clarified by applying 2 ns time resolution. The results show that He emission peak is followed by N_2 (with about 3 ns delay) and afterwards by N_2^+, which is further delayed by 3 ns. At the same time, the growth of O emission is much slower (having roughly 30 ns delay). The time separation between N_2, N_2^+ and O emission growth disappears upon the air addition. In the case of air admixture the N_2, N_2^+ and O emission increases synchronously, whereas in the case of vapor admixture the synchronous growth persists but the emission evolution is additionally delayed by 10 ns (see Fig. 10, next section). The presented time-resolved OES data reveal important stages of the discharge evolution, including the electron avalanche formation and emission lines dynamics. The further analysis of the ro-vibrational excitation is undertaken below.

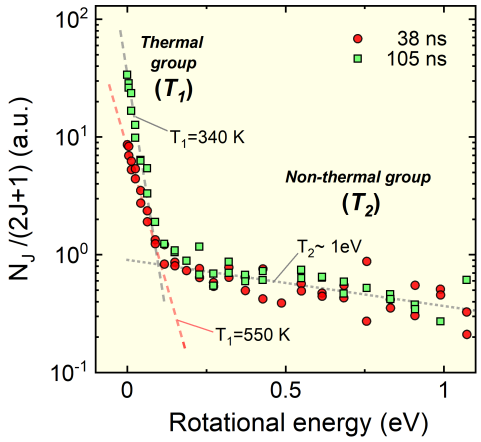

FIG. 11. Rotational distributions corresponding to OH (A-X, 0-0) emission band measured in the discharge area at two time delays. The characteristic temperatures, T_1 (corresponding to thermal OH group) and T_2 (non-thermal group) are shown. He + 15 v.u. gas mixture is used.

C. Rotational dynamics

1. N_2 and N_2^+ molecules

Thermalization in the gas is defined by the translational-translational (T-T) energy exchange and the corresponding characteristic time, which is below 150 ps for the gases used in this work [82]. Since this time is considerably shorter than the plasma pulse width in our case, the gas is always in translational equilibrium during the plasma interval. The rate coefficients for the main energy exchange channels are summarized in Table IV.

The gas temperature (T_{gas}) is often deduced from rotational temperature of the diatomic molecules, assuming that the distribution of rotational level populations is in equilibrium with gas kinetic motion. In our case the rotational distributions for examined molecules (namely N_2(C), N_2^+(B) and OH(A) states) reveal different behavior. Remarkably, N_2^+ ions demonstrate abrupt increase in T_{rot} at the early stage, see Fig. 9. The start of T_{rot} growth was hardly measurable in some cases due to the weak N_2^+ emission intensity. Its peak, however, was always clearly localized *preceding* the He emission peak by few ns, as clear from Fig. 10. After the peak T_{rot} decays in about 12 ns and gets saturated in about 50 ns. Both the peak and the plateau values of T_{rot} remain rather insensitive to air admixture.

At the same time, the rotational excitation of N_2 remains unaffected by the plasma pulse, always corresponding to T_{rot} of about 300-320 K, as show in Figs. 9 and 10. The characteristic time of R-T relaxation estimated for N_2 - He collisions based on the available cross-section data [83] is about 0.3 ns, which is shorter than plasma pulse, so T_{rot} should follow T_{gas} in this case. At the same time, the excitation of N_2 rotational levels by electrons happens with a much lower rate corresponding to the e-R relaxation time of about 90 ns (estimated using the LoKI-B Solver [75] assuming the electron density $n_e = 5{\cdot}10^{15}$ cm^{-3}, as measured in our discharge using Stark broadening of He and H_β emission lines [74]). This time is much longer than the pulse duration, so the e-V excitation mechanism cannot be fully activated during the plasma phase. Based on these arguments we should assume that the gas temperature remains in the range of 300-320 K through the entire plasma cycle. This result corroborates with the data obtained with N_2 rotational band by Laroussi and Lu [46] for a He atmospheric plasma jet operating with 500 ns pulses.

The observed jump in rotational excitation of N_2^+ molecules may be a result of interaction between N_2 molecules and FIW wavefront containing energetic electrons, leading to the direct electron impact ionization of N_2, likely accompanied by rotational excitation. Another possibility for this jump may be the charge exchange reaction with He_2^+ ions, as studied by Piper et al. [88] and later by Endoh et al. [89]. In the latter case the role of these reactions in formation and enhanced rotational excitation of N_2^+(B) state is demonstrated without giving an explanation of this effect. At the same time, the role of He(2s ^{3}S) metastable state in such rotational excitation is found minor [89]. Following this logic, the N_2 molecules which do not experience charge exchange with He_2^+ ions should not reveal any additional rotational excitation. This is consistent with our results, where any time perturbations in T_{rot} of N_2 is registered, which additionally approves our suggestion about proximity of this temperature to T_{gas}.

In our case N_2 remains excited vibrationally, showing comparable T_{vibr} values in the discharge and post-discharge, as shown below. This fact confirms strong excitation in the wavefront, accompanied by e-V and V-V energy transfer and ionization.

2. OH molecules

Unlike the N_2 and N_2^+ cases, the OH rotational distributions in the discharge reveal double Boltzmann slope, as shown in Fig. 11. This effect is well-described in literature for OH [66, 67, 90], N_2 [91], H_2 [92] and CH [93] molecules. In the case of OH it be a result of the electron impact excitation of singlet water states, as discussed by Möhlmann et al. [94]. It may lead to the production of OH with low and high rotational energy, depending on the water bonds orientation, thus corresponding to different rotational energy groups. The low energy OH group with low rotational numbers ($J < 10$ typically) is often thermalized with kinetic gas motion since the R-T exchange rates are much higher for lower rotational states [93].

In our case the OH rotational temperature T_1 (thermal group) ranges between 350 K and 800 K, whereas the values of T_2 (non-thermal group) are always above 1 eV.

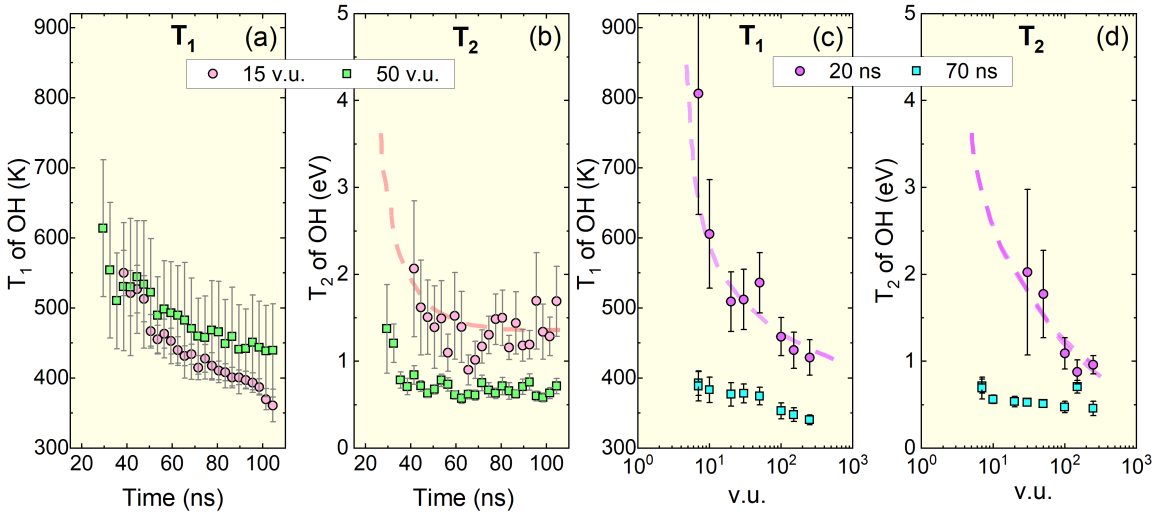

FIG. 12. Dynamics of rotational temperatures corresponding to thermalized OH group, T_1 (a) and non-thermalized group, T_2 (b) measured at two water vapor admixtures. The behavior of T_1 (c) and T_2 (d) temperatures as a function of water vapor admixture at two fixed time delays.

The dynamics of both T_1 and T_2 is quite similar, as shown in Fig. 12(a,b). In spite of the large error bars in some cases (caused by low OH intensity), the time relaxation of both T_1 and T_2 is clear. At the beginning T_1 is about 600 K slowly decaying afterwards, with the decay time few times longer than that observed for T_{rot} of N_2^+ (see Fig. 9), which is likely a result of different rotational relaxation rates for these species in He. The estimation gives the R-T relaxation time for OH - He collisions of about 5 ns [84, 85] which is much shorter than the observed decay time for T_1 and the slow temperature relaxation should likely be ascribed to the additional rotational pumping in the CCP plasma. The thermalization of OH rotational excitation with gas motion is expected at about 1 μs in our conditions.

The T_2 temperature, on the other hand, reaches the plateau rather quickly, in about 50 ns, especially at high water vapor admixture, see Fig. 12(b). At high vapor content T_2 is clearly lower, resulting in a shrinking of the gap between T_1 and T_2 and thus indicating higher discharge thermalization, see Fig. 12(b). Both T_1 and T_2 decay when more water vapor is added, as clarified in Fig. 12(c,d), approving this fact.

IV. POST-DISCHARGE AND JET AREAS

A. Emission spectra

In the ns- jet discharges, as a result of ionization waves propagation, the energetic electrons in the wavefront may participate to gas excitation and ionization [25] also leading to formation of the He excited and metastable states as well as the vibrationally excited molecules. In He-based discharges, the metastable atoms (He^{met}, $2s\,^3S_1$ state [95]) generated during the plasma pulse are also strong candidates for Penning ionization (He^{met} + N_2 → He + N_2^+) and vibrational excitation. Thus, we may assume that inside the quartz tube both discharge and post-discharge kinetics may be combined in our case.

The spectra taken in the post-discharge and jet (the emitting part of the effluent outside the tube) areas are rather different, as compared to the discharge core. As shown in Fig. 13, mainly the N_2^+ emission dominates in the post-discharge case, whereas He and N_2 emission is suppressed. In the jet area, due to the influence of ambient air, the relative contribution of the N_2 Second Positive System emission gets strong again, while He emission is still insignificant. Overall, the N_2 emission undergoes about threefold decrease in the jet region, He is suppressed roughly by a factor of ten, whereas the emission of N_2^+ and O drops by more than an order of magnitude (see the supplementary data, Fig. S5).

The reason for emission suppression in the post-discharge (compared to the discharge area) is absence of electron avalanche and much lower electron density [74]. The electrons in the ionization wavefront are still energetic since they undergo acceleration in the high electric field of a wavefront [96]. These facts result in a weak He excitation in the tube. Instead, the emission from N_2^+ molecular ions dominates in post-discharge, see Fig. 13, implying that electron energy may be mainly channelized for N_2 vibrational excitation and ionization, being not sufficient for He excitation.

B. Ro-vibrational dynamics

The rotational and vibrational temperature dynamics in the post-discharge and jet areas is summarized in Fig. 14 with first three panels representing the discharge,

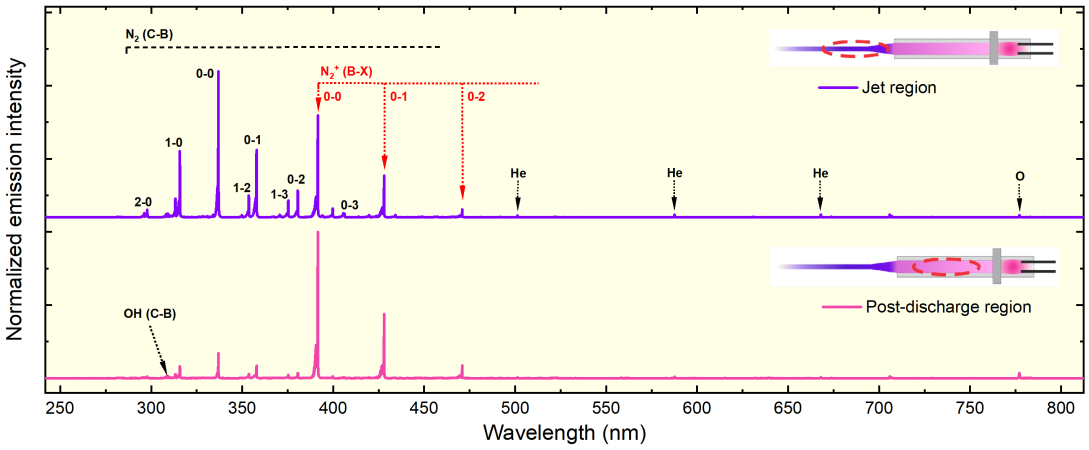

FIG. 13. Emission spectra acquired in the post-discharge and jet regions (normalized to 1) using 1 μs of the ICCD gate width. About 25 mm long area is covered by fibre aperture: in the middle of the quartz tube (for post-discharge) and right after the tube edge (for jet), as shown in the insets. He with 0.1% of air admixture is used.

post-discharge and jet areas, respectively, and the last one summarizing T_{vibr} of the $N_2(C)$ state. The He and N_2 emission peaks shifting in time are given for reference; they additionally confirm the FIW propagation in the tube. The corresponding FIW propagation velocity does not exceed about $5{\cdot}10^5$ m/s (see also Part II [74]).

The discharge region, shown in Fig. 14(a), is characterized by a peak of T_{rot} of N_2^+ reaching about 650 K and slightly preceding the He emission peak, as well as by a nearly constant T_{rot} of N_2, as discussed above.

In the post-discharge, Fig. 14(b), the T_{rot} of N_2 still remains constant and nearly equal to that found in the discharge. In this case the emission has been collected from about 25 mm long area in the middle of the discharge tube using longer ICCD gate (typically 30 ns). Since the passing time for the FIW front does not exceed roughly 10 ns in our case the additional e-R excitation in the gas (characteristic time of 90 ns, see Table IV) does not happen and T_{rot} of N_2 remains equal to gas temperature. At the same time, T_{rot} of N_2^+ in the post-discharge starts decaying from a lower value (about 450 K) pointing out on a weaker rotational excitation. After the relaxation it is clearly lower in the post-discharge ($\approx$320 K vs. 380 K in the discharge). The decay time of N_2^+ rotational temperature in the post-discharge is longer than both the value found in the discharge and the R-T time for N_2-He collisional exchange (see Table IV), so the additional rotational excitation of N_2 ions in the FIW tail may be suggested, as the tail represents a conductive channel formed after the wavefront [25, 96]. After the decay T_{rot} of both N_2 and N_2^+ reaches nearly the same value, about 320 K, indicating higher thermalization, compared to the discharge area.

In the jet (effluent) area, Fig. 14(c), rotational excitation of N_2^+ also correlates with the moment of He peak appearance confirming FIW propagation outside the tube. The rotational excitation is registered at about 100 ns corresponding to about 400 K, showing a decent time relaxation. The T_{rot} of N_2 still remains about 300 K in this case. The rotational analysis of the OH bands was not performed in the post-discharge and jet regions due to low emission intensity and overlapping with N_2 (C-B, 2-1) rotational band [64].

Finally, the vibrational temperature of $N_2(C)$ state shows almost linear decay in the discharge, post-discharge and jet areas, see Fig. 14(d). The estimated e-V exchange time in the discharge area is about 45 ns (based on the available e-V rate coefficients [75], $n_e = 5{\cdot}10^{15}$ cm^{-3} [74] and reduced electric field E/N = 100 Td. The last quantity is determined based on the electric field value measured in the discharge area using He emission lines splitting [74]). Since the plasma pulse duration is only 10 ns, N_2 remains underexcited vibrationally. Moreover, the visible decay of T_{vibr} (about 50 ns) is much shorter than the estimated V-T relaxation time defined by collisions with He atoms, for which the estimation gives about 6 ms [82, 86]. At the same time, the influence of collisions with N_2 and O_2 is negligible at small air admixtures [82, 87]. Since the apparent vibrational relaxation happens much faster, yet another mechanism for this process should be suggested.

V. CONCLUSIONS

In the first part of our study, devoted to the electrical and optical characterization of a ns- jet discharge, few important results related to the discharge dynamics are obtained. We found that the discharge current shows a sharp 10 ns peak which as a result of gas breakdown and plasma channel formation in the electrode gap. The current peak value, width and risetime are sensitive to the pulse repetition rate and the air admixture. A faster current growth is found at higher air admixtures indicating quicker breakdown, whereas the peak current decreases at the same time. Contrary, the peak current

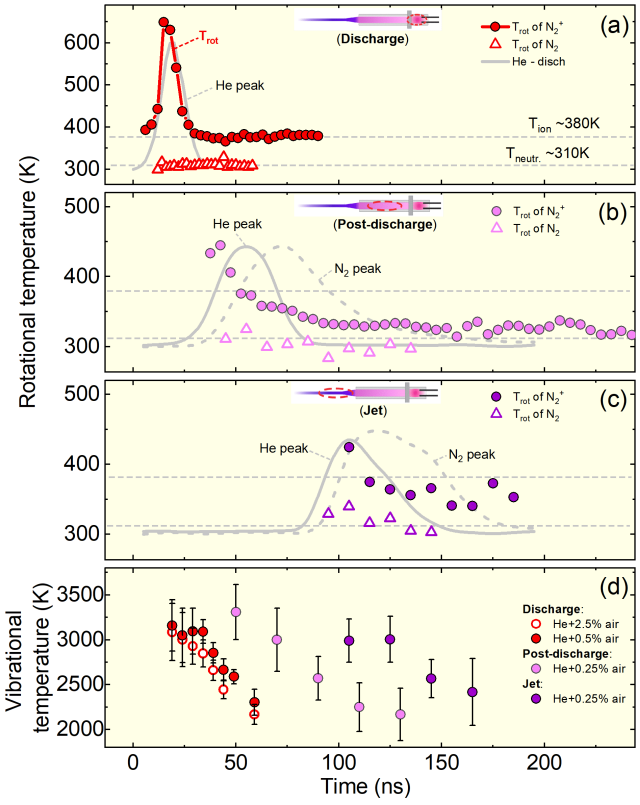

FIG. 14. Time-resolved evolution of the rotational temperature (of N_2 and N_2^+) in the plasma (a), post-discharge (b) and jet (c) regions, along with the evolution of N_2 vibrational temperature in the same regions (d). Evolution of the normalized He (587.6 nm) and N_2 (380.5 nm) emission lines are given for reference. The horizontal dashed lines indicate the values of T_{rot} for N_2 and N_2^+ measured in the discharge area.

increases dramatically at low pulse repetition rate, indicating harder breakdown, which is likely related to a lower residual charge in the the discharge gap.

The emission spectra show different spectral lines domination in the discharge, post-discharge and jet zones. In the electrode gap, as a result of electron abundance, the main gas species get excited by electron impact, a process which dominates for a short time (10-20 ns), comparable to the current peak width. This is related to both low-threshold (such as N_2) and high-threshold (such as He) excited states resulting in a strong emission of N_2, N_2^+ and He.

In the post-discharge (tube) the emission of He is strongly suppressed pointing out on a much weaker electron excitation, primarily as a result of low electron density in the ionization wavefronts. The time-resolved data confirm ionization wave propagation in the post-discharge and jet, resulting in the vibrational excitation and ionization of N_2 molecules. The energy of electrons in the FIW front is supposed to be channelized toward ionization and excitation of electronic states, which is confirmed by domination of N_2^+ emission in the tube.

Finally, in the effluent area, as a result of the wavefront entering into the ambient air, the emission bands from the Second Positive System of N_2 rise again, which is accompanying by an overall emission intensity drop.

In all the discharge regions and during the whole discharge cycle gas temperature remains nearly constant, of about 300-320 K, as found by N_2 rotational distributions. Such a low temperature is consistent with earlier studies, being a result of a). sub-ns T-T thermalization time, b) shorter than plasma pulse R-T characteristic time of N_2-He interaction (about 0.3 ns) and c) slow e-R, e-V and (especially) V-T relaxation processes having characteristic time considerably longer than the plasma pulse. We should additionally note that the rotational temperature of N_2^+ demonstrates a clear jump during the plasma pulse, overtaking He emission in the gap, which may imply a fast rotational pumping (taking place before electron avalanche), an interesting effect requiring further attention.

Finally, the water vapor addition result in OH radical formation in the discharge, which rotational distributions reveal two-temperature slope, corresponding to thermal and non-thermal OH groups in plasma, which is a rather typical outcome for water vapor containing discharges. The low-temperature group reveals somewhat higher temperatures as compared to those found by N_2 molecules, indicating (again) certain rotational non-equilibrium in the gas.

This work clarifies several important aspects of the ns- jet discharge evolution and ro-vibrational thermalization, both in the temporal and in spatial domains. For further understanding of the discharge behavior the additional knowledge might be required, in particular the one related to ionization wave dynamics, kinetics of He metastables, plasma density and electric field dynamics. Some of these questions are discussed in the Part II of this study [74].

ACKNOWLEDGMENTS

This work is supported by the JSPS KAKENHI Tokusui project (grant 19H05462). We sincerely thank Dr. Tiago Silva (Instituto Superior Técnico, Universidade de Lisboa, Portugal) for providing the key rate coefficients and related literature sources, as well as Dr. Jan Voráč (former affiliation: Masaryk University, Brno, Czech Republic) for the fruitful discussions related to usage of the Massive OES software and OH spectra fitting.

[1] V. D. Rusanov, A. A. Fridman, and G. V. Sholin, Uspekhi Fiz. Nauk **134**, 185 (1981).

[2] A. A. Fridman, *Plasma Chemistry* (Cambridge University Press, Cambridge, 2005).

[3] S. Huang, T. Li, Z. Zhang, and P. Ma, Applied Energy **251**, 113358 (2019).

[4] N. Britun, V. Gamaleev, and M. Hori, Plasma Sources Science and Technology **30**, 08LT02 (2021).

[5] P. J. Bruggeman, *Low Temperature Plasma Technology*, edited by P. K. Chu and X. Lu (Taylor and Francis, London, 2014).

[6] S. Bozhenkov, S. Starikovskaia, and A. Starikovskii, Combustion and Flame **133**, 133 (2003).

[7] A. Starikovskiy and N. Aleksandrov, Progress in Energy and Combustion Science **39**, 61 (2013).

[8] K. C. Opacich, T. M. Ombrello, J. S. Heyne, J. K. Lefkowitz, R. J. Leiweke, and K. Busby, Proceedings of the Combustion Institute **38**, 6615 (2021).

[9] H. Zhang, Y. Wu, and Y. Li, International Journal of Heat and Fluid Flow **80**, 108502 (2019).

[10] S. Meropoulis, G. Rassias, V. Bekiari, and C. Aggelopoulos, Separation and Purification Technology **274**, 119031 (2021).

[11] C. Schroeder, W. Schroeder, S. Yang, A. Nystrom, Z. Cai, S. Subramanian, S. Li, M. A. Gundersen, and S. B. Cronin, Fuel Processing Technology **208**, 106521 (2020).

[12] M. Gromov, K. Leonova, N. De Geyter, R. Morent, R. Snyders, N. Britun, and A. Nikiforov, Plasma Sources Science and Technology **30**, 065024 (2021).

[13] C. Montesano, S. Quercetti, L. M. Martini, G. Dilecce, and P. Tosi, Journal of CO_2 Utilization **39**, 101157 (2020).

[14] C. Montesano, M. Faedda, L. M. Martini, G. Dilecce, and P. Tosi, Journal of CO_2 Utilization **49**, 101556 (2021).

[15] T. Tang, H. Lee, H. Kim, G. Kim, B. Lee, H. Kim, and H. Lee, Current Applied Physics **29**, 9 (2021).

[16] M. Laroussi and T. Akan, Plasma Processes and Polymers **4**, 777 (2007).

[17] L. Li, C. Leys, N. Britun, R. Snyders, and A. Y. Nikiforov, IEEE Transactions on Plasma Science **42**, 2752 (2014).

[18] Y. L. Stankevich and V. G. Kalinin, Proc. USSR Acad. Sci. **177**, 72 (1967), (in Russian).

[19] V. F. Tarasenko, C. Zhang, E. K. Baksht, A. G. Burachenko, T. Shao, D. V. Beloplotov, M. I. Lomaev, P. Yan, A. V. Kozyrev, and N. S. Semeniuk, Matter and Radiation at Extremes **2**, 105 (2017).

[20] V. F. Tarasenko, E. K. Baksht, A. G. Burachenko, I. D. Kostyrya, M. I. Lomaev, and D. V. Rybka, Plasma Devices and Operations **16**, 267 (2008).

[21] R. C. Noggle, E. P. Krider, and J. R. Wayland, Journal of Applied Physics **39**, 4746 (1968).

[22] C. T. R. Wilson, Proceedings of the Physical Society of London **37**, 32D (1924).

[23] C. T. R. Wilson, Mathematical Proceedings of the Cambridge Philosophical Society **22**, 534–538 (1925).

[24] S. B. Alekseev, V. M. Orlovskii, V. F. Tarasenko, A. N. Tkachev, and S. I. Yakovlenko, Technical Physics Letters **29**, 679 (2003).

[25] L. M. Vasilyak, S. V. Kostyuchenko, N. N. Kudryavtsev, and I. V. Filyugin, Physics-Uspekhi **37**, 247 (1994).

[26] N. B. Anikin, S. V. Pancheshnyi, S. M. Starikovskaia, and A. Y. Starikovskii, Journal of Physics D: Applied Physics **31**, 826 (1998).

[27] N. B. Anikin, S. M. Starikovskaia, and A. Y. Starikovskii, Journal of Physics D: Applied Physics **35**, 2785 (2002).

[28] K. Takashima, I. V. Adamovich, Z. Xiong, M. J. Kushner, S. Starikovskaia, U. Czarnetzki, and D. Luggenhölscher, Physics of Plasmas **18**, 083505 (2011).

[29] M. Yousfi, O. Eichwald, N. Merbahi, and N. Jomaa, Plasma Sources Science and Technology **21**, 045003 (2012).

[30] S. Wu, X. Lu, and Y. Pan, Physics of Plasmas **21**, 073509 (2014).

[31] S. Wu, X. Lu, Y. Yue, X. Dong, and X. Pei, Physics of Plasmas **23**, 103506 (2016).

[32] M. Popov, I. Kochetov, A. Starikovskiy, and N. Aleksandrov, Combustion and Flame **233**, 111611 (2021).

[33] M. Uddi, N. Jiang, I. V. Adamovich, and W. R. Lempert, Journal of Physics D: Applied Physics **42**, 075205 (2009).

[34] S. V. Pancheshnyi, S. M. Starikovskaia, and A. Y. Starikovskii, Journal of Physics D: Applied Physics **32**, 2219 (1999).

[35] D. Z. Pai, G. D. Stancu, D. A. Lacoste, and C. O. Laux, Plasma Sources Science and Technology **18**, 045030 (2009).

[36] D. A. Sorokin, D. V. Beloplotov, V. F. Tarasenko, and E. K. Baksht, Applied Physics Letters **118**, 224101 (2021).

[37] S. Hübner, S. Hofmann, E. M. van Veldhuizen, and P. J. Bruggeman, Plasma Sources Science and Technology **22**, 065011 (2013).

[38] W. V. Gaens, S. Iseni, A. Schmidt-Bleker, K.-D. Weltmann, S. Reuter, and A. Bogaerts, New Journal of Physics **17**, 033003 (2015).

[39] J. Winter, R. Brandenburg, and K.-D. Weltmann, Plasma Sources Science and Technology **24**, 064001 (2015).

[40] G. B. Sretenović, O. Guaitella, A. Sobota, I. B. Krstić, V. V. Kovačević, B. M. Obradović, and M. M. Kuraica, Journal of Applied Physics **121**, 123304 (2017).

[41] S. Yonemori and R. Ono, Biointerphases **10**, 029514 (2015).

[42] J. Schäfer, F. Sigeneger, R. Foest, D. Loffhagen, and K.-D. Weltmann, European Physical Journal D **60**, 531 (2010).

[43] K. P. Arjunan, A. Obrusník, B. T. Jones, L. Zajíčková, and S. Ptasinska, Plasma Processes and Polymers **13**, 1089 (2016).

[44] X. Lu, M. Laroussi, and V. Puech, Plasma Sources Science and Technology **21**, 034005 (2012).

[45] Y. Morabit, M. I. Hasan, R. D. Whalley, E. Robert, M. Modic, and J. L. Walsh, European Physical Journal D **75**, 32 (2021).

[46] M. Laroussi and X. Lu, Applied Physics Letters **87**, 113902 (2005).

[47] X. Lu, D. Liu, Y. Xian, L. Nie, Y. Cao, and G. He, Physics of Plasmas **28**, 100501 (2021).

[48] E. R. W. V. Doremaele, V. S. S. K. Kondeti, and P. J. Bruggeman, Plasma Sources Science and Technology **27**, 095006 (2018).

[49] S. Hübner, J. S. Sousa, V. Puech, G. M. W. Kroesen, and N. Sadeghi, Journal of Physics D: Applied Physics **47**, 432001 (2014).

[50] C. Jiang, J. Miles, J. Hornef, C. Carter, and S. Adams, Plasma Sources Science and Technology **28**, 085009 (2019).

[51] F. Wu, J. Li, Y. Xian, X. Tan, and X. Lu, Plasma Processes and Polymers **18**, 2100033 (2021).

[52] A. M. Lietz and M. J. Kushner, Journal of Applied Physics **124**, 153303 (2018).

[53] Z. Xiong, X. Lu, Y. Xian, Z. Jiang, and Y. Pan, Journal of Applied Physics **108**, 103303 (2010).

[54] M. van der Schans, P. Böhm, J. Teunissen, S. Nijdam, W. IJzerman, and U. Czarnetzki, Plasma Sources Science and Technology **26**, 115006 (2017).

[55] P. Olszewski, E. Wagenaars, K. McKay, J. W. Bradley, and J. L. Walsh, Plasma Sources Science and Technology **23**, 015010 (2014).

[56] D. Kong, P. Zhu, F. He, R. Han, B. Yang, M. Wang, and J. Ouyang, Journal of Applied Physics **129**, 103303 (2021).

[57] G. B. Sretenović, I. B. Krstić, V. V. Kovačević, B. M. Obradović, and M. M. Kuraica, Journal of Physics D: Applied Physics **47**, 102001 (2014).

[58] S. Hofmann, A. F. H. van Gessel, T. Verreycken, and P. Bruggeman, Plasma Sources Science and Technology **20**, 065010 (2011).

[59] T. L. Chng, A. Brisset, P. Jeanney, S. M. Starikovskaia, I. V. Adamovich, and P. Tardiveau, Plasma Sources Science and Technology **28**, 09LT02 (2019).

[60] K. Orr, Y. Tang, M. S. Simeni, D. van den Bekerom, and I. V. Adamovich, Plasma Sources Science and Technology **29**, 035019 (2020).

[61] V. Gamaleev, N. Shimizu, and M. Hori, Review of Scientific Instruments **93**, 053503 (2022).

[62] N. Shimizu, T. Sekiya, K. Iida, Y. Imanishi, M. Kimura, and J. Nishizawa, in *2004 Proceedings of the 16th International Symposium on Power Semiconductor Devices and ICs* (2004) pp. 281–284.

[63] E. I. Asinovskiy, L. M. Vasilyak, and V. V. Markovets, Teplofizika visokih temperatur **21**, 371 (1983), (in Russian).

[64] R. W. B. Pearce and A. G. Gaydon, *The Identification of Molecular Spectra*, 2nd ed. (Chapmann and Hall, London, 1950).

[65] J. Voráč, P. Synek, L. Potočňáková, J. Hnilica, and V. Kudrle, Plasma Sources Science and Technology **26**, 025010 (2017).

[66] J. Voráč, P. Synek, V. Procházka, and T. Hoder, Journal of Physics D: Applied Physics **50**, 294002 (2017).

[67] J. Voráč, L. Kusýn, and P. Synek, Review of Scientific Instruments **90**, 123102 (2019).

[68] J. Luque and D. Crosley, LIFBASE: Database and Spectral Simulation Program (Version 2.1.1) (1999).

[69] N. Britun, T. Godfroid, and R. Snyders, Journal of CO_2 Utilization **41**, 101239 (2020).

[70] A. Lofthus and P. H. Krupenie, J. Phys. Chem. Ref. Data **6**, 113 (1977).

[71] Y. P. Raizer, *Gas Discharge Physics*, 1st ed., edited by J. E. Allen (Springer-Verlag, Berlin Heidelberg, 1991).

[72] H. J. Reich, *Theory and applications of electron tubes*, 2nd ed. (McGraw Hill, New York, London, 1944).

[73] D. A. Lacoste, A. Bourdon, K. Kuribara, K. Urabe, S. Stauss, and K. Terashima, Plasma Sources Science and Technology **23**, 062006 (2014).

[74] N. Britun, P. Dennis Christy, V. Gamaleev, S.-N. Hsiao, and M. Hori, Plasma Sources Science and Technology (2022), *Submitted simultaneously*.

[75] A. T. del Caz, V. Guerra, D. Gonçalves, M. L. da Silva, L. Marques, N. Pinhão, C. D. Pintassilgo, and L. L. Alves, Plasma Sources Science and Technology **28**, 043001 (2019).

[76] Q. Li, W.-C. Zhu, X.-M. Zhu, and Y.-K. Pu, Journal of Physics D: Applied Physics **43**, 382001 (2010).

[77] A. Catherinot and B. Dubreuil, Journal de Physique Colloques **40**, C7 (1979).

[78] B. Dubreuil and A. Catherinot, Journal de Physique Colloques **40**, C7 (1979).

[79] S. Pancheshnyi, S. Starikovskaia, and A. Starikovskii, Chemical Physics Letters **294**, 523 (1998).

[80] E. Gat, N. Gherardi, S. Lemoing, F. Massines, and A. Ricard, Chemical Physics Letters **306**, 263 (1999).

[81] Chemical Physics Letters **444**, 39 (2007).

[82] M. Capitelli, C. M. Ferreira, B. F. Gordiets, and A. I. Osipov, *Plasma Kinetics in Atmospheric Gases* (Springer, Bari, Lisbon, Moscow, 2000).

[83] A. E. Belikov, R. G. Sharafutdinov, and A. V. Storozhev, Chemical Physics **213**, 319 (1996).

[84] J. Kłos, F. Lique, and M. Alexander, Chemical Physics Letters **445**, 12 (2007).

[85] A. D. Esposti, A. Berning, and H. Werner, The Journal of Chemical Physics **103**, 2067 (1995).

[86] A. J. Banks, D. C. Clary, and H. Werner, The Journal of Chemical Physics **84**, 3788 (1986).

[87] M. Cacciatore, A. Kurnosov, and A. Napartovich, The Journal of Chemical Physics **123**, 174315 (2005).

[88] L. G. Piper, L. Gundel, J. E. Velazco, and D. W. Setser, The Journal of Chemical Physics **62**, 3883 (1975).

[89] M. Endoh, M. Tsuji, and Y. Nishimura, The Journal of Chemical Physics **79**, 5368 (1983).

[90] P. J. Bruggeman, N. Sadeghi, D. C. Schram, and V. Linss, Plasma Sources Science and Technology **23**, 023001 (2014).

[91] D. W. Setser, D. H. Stedman, and J. A. Coxon, The Journal of Chemical Physics **53**, 1004 (1970).

[92] S. Briefi and U. Fantz, Plasma Sources Science and Technology **29**, 125019 (2020).

[93] J. L. Cooper and J. C. Whitehead, J. Chem. Soc., Faraday Trans. **89**, 1287 (1993).

[94] G. Möhlmann, C. Beenakker, and F. de Heer, Chemical Physics **13**, 375 (1976).

[95] I. Korolov, M. Leimkühler, M. Böke, Z. Donkó, V. S. von der Gathen, L. Bischoff, G. Hübner, P. Hartmann, T. Gans, Y. Liu, T. Mussenbrock, and J. Schulze, Journal of Physics D: Applied Physics **53**, 185201 (2020).

[96] W. P. Winn, Journal of Applied Physics **38**, 783 (1967).